ACS APPLIED MATERIALS & INTERFACES

Research Article

Cite This: ACS Appl. Mater. Interfaces 2019, 11, 47929−47938

www.acsami.org

Layer-by-Layer Assembly of Polyaniline Nanofibers and MXene Thin-Film Electrodes for Electrochemical Energy Storage

Junyeong Yun,[†,‡] Ian Echols,[†] Paraskevi Flouda,[§] Shaoyang Wang,[†] Alexandra Easley,[§] Xiaofei Zhao,[†] Zeyi Tan,[§] Evan Prehn,[§] Goangseup Zi,[‡] Miladin Radovic,[§] Micah J. Green,[†,§] and Jodie L. Lutkenhaus*[,†,§]

[†]Artie McFerrin Department of Chemical Engineering and [§]Department of Materials Science and Engineering, Texas A&M University, College Station, Texas 77843, United States

[‡]Department of Civil, Environmental and Architectural Engineering, Korea University, Seoul 02841, Republic of Korea

Supporting Information

ABSTRACT: The growing demand for compact energy storage devices may be met through the use of thin-film microbatteries, which generally rely on charge storage in thin or conformal layers. A promising technique for creating thin-film electrodes is layer-by-layer (LbL) assembly, based on the alternating adsorption of oppositely charged species to a surface to form a nanostructured electrode. Thin-film energy storage devices must have a high energy density within a limited space, so new electrode structures, materials, and assembly methods are important. To this end, both two-dimensional MXenes and polyaniline nanofibers (PNFs) have shown promising energy storage properties. Here, we report on the LbL assembly of positively charged PNFs and negatively charged $Ti_3C_2T_x$ MXenes into hybrid electrodes for thin-film energy storage devices. The successful assembly is demonstrated in which MXenes and PNFs are deposited in films of 49 nm/layer pair thickness. The resulting composition was 77 wt % PNFs and 23 wt % MXenes. The charge storage process was deconvoluted into faradaic/non-faradaic contributions and separated into contributions from PNFs and MXenes. A sandwich cell showed a maximum areal capacity, energy, and power of 17.6 μA h cm^{-2}, 22.1 μW h cm^{-2}, and 1.5 mW cm^{-2}, respectively, for PNF/MXene multilayers of about 2 μm thickness. This work suggests the possibility of using LbL PNF/MXene thin films as electrode materials for thin-film energy storage devices used in next-generation small electronics.

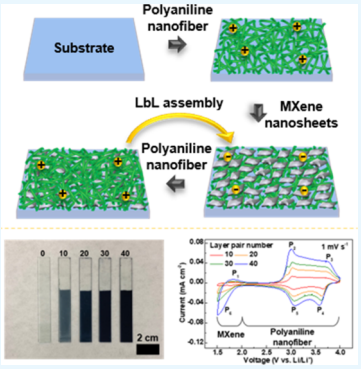

KEYWORDS: *layer-by-layer assembly, MXene, polyaniline nanofiber, thin-film energy storage*

1. INTRODUCTION

Along with the fourth industrial revolution, the emergence of the Internet of Things has greatly stimulated the design of high-tech small-sized electronic devices.[1,2] Subsequently, the demand for microscale energy storage devices to enable the miniaturization and portability of electronic devices has increased.[3,4] Although thin-film microbatteries and electrochemical capacitors show promise to meet this demand,[5−8] many challenges still remain. For example, the electrodes should be easy to deposit, have controllable thickness, and provide high energy and power. In this regard, layer-by-layer (LbL) assembly of MXene nanosheets and polyaniline nanofibers (PNFs) into thin-film electrodes is of interest.

MXenes are an emerging class of two-dimensional (2D) early transition-metal carbides and carbonitrides that can be obtained by selective etching and exfoliation of MAX phases.[9,10] M is an early transition metal (e.g., Sc, Ti, Zr, Hf, V, Nb, Ta, Cr, and Mo), X is carbon or nitrogen, A is generally Al or Ga, or other 13−16 group elements, and T represents the surface terminal groups (=O, −OH, and/or −F).[11] $Ti_3C_2T_x$ MXenes possess outstanding conductivity (~10 000 S cm^{-1} for freestanding films), electrochemical properties, high surface area, and functionalized surfaces.[12] The latter feature leads to hydrophilic nanosheets that are readily dispersible in water. Since their discovery, MXenes have been used for a variety of applications including sensing, energy storage, electromagnetic interference shielding, and optoelectronics.[13−16] In particular, MXene nanosheets have been actively studied as electrode materials for batteries and supercapacitors.[17−19] However, MXenes, such as other 2D layered nanomaterials, can restack and agglomerate during processing, which interferes with electrolyte ion diffusion and consequently limits the electrochemical reaction rate.[20] In this work, we propose that conductive polymers can be used to prevent MXene stacking, while providing additional electrochemical activity and conductive pathways.

Conductive polymers (e.g., polythiophene, polypyrrole, and polyaniline) have been actively studied as electrode materials for electrochemical energy storage devices.[21−23] Among them, polyaniline, a p-type conjugated polymer, has drawn attention

Received: September 15, 2019
Accepted: November 27, 2019
Published: November 27, 2019

DOI: 10.1021/acsami.9b16692
ACS Appl. Mater. Interfaces 2019, 11, 47929−47938

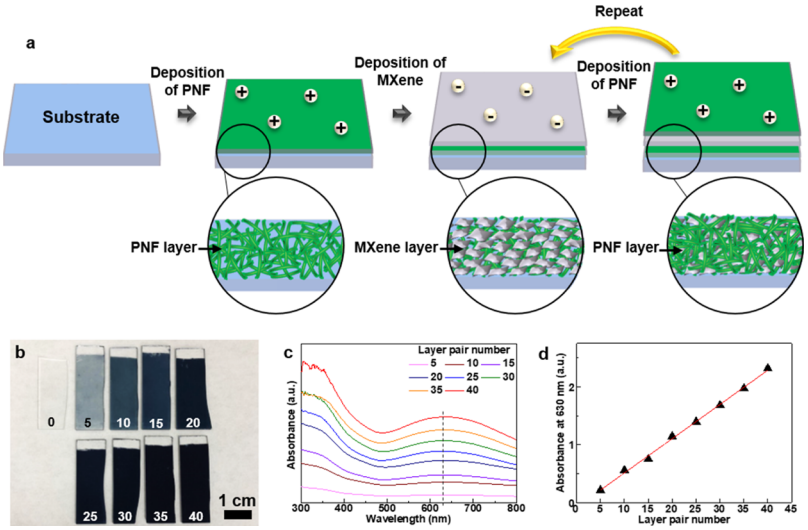

Figure 1. (a) Schematic illustration of the PNF/MXene LbL assembly process. (b) Image of glass substrates coated with various numbers of LPs. (c) UV−vis spectra of PNF/MXene multilayers on glass. The dotted line indicates λ = 630 nm. (d) Absorbance value at 630 nm vs number of LPs.

because of its high theoretical capacity (294 mA h g^{-1} when fully doped), conductivity (2−5 S cm^{-1} in emeraldine salt form), low cost, and facile synthesis methods.[24−27] Polyaniline stores charge through a pseudocapacitive doping mechanism in which polyaniline is oxidized and reduced causing anions to move into and out of the electrode.[28] From this point of view, PNFs are very promising because they provide a porous structure and have a larger specific surface area (33.6 m^2 g^{-1}).[29,30] PNFs can be synthesized rapidly in water to yield a colloidally stable aqueous dispersion,[31] which facilitates water-based processing and assembly.

LbL assembly is a promising method for creating conformal thin-film electrodes.[32−34] LbL assembly is a sequential, alternating, aqueous adsorption process for materials with complementary functional groups using hydrogen bonding, electrostatic, or other intermolecular interactions.[35,36] LbL assembly produces conformal coatings on a wide range of material surface topographies such as on planar surfaces, on spherical particles, within pores, or on fabrics, which is otherwise not possible with doctor blading or spin-coating fabrication methods. In addition, LbL assembly has been used as a method to produce mechanically stable films in various applications such as antifogging coatings, supercapacitors, biosensors, and many others.[37−41] Previously, LbL assembly was used to produce electrodes containing reduced graphene oxide, single-walled and multiwalled carbon nanotubes, V_2O_5, and polyelectrolytes on fabric, glass, metal wire, PET, polydimethylsiloxane, and silicon wafer substrates.[4,10,16,25,42,43]

In this study, we report on thin-film PNF/MXene LbL electrodes for use in thin-film electrochemical energy storage. Because PNF/MXene electrodes have not yet been reported as electrode materials, we first describe the LbL assembly process of positively charged one-dimensional PNFs and negatively charged 2D MXene nanosheets. We use sodium L-ascorbate to prevent oxidation of the MXene sheets.[44] LbL growth was investigated using profilometry, UV−vis spectroscopy, and quartz crystal microbalance. The structure and chemical properties of the PNF/MXene LbL electrode and its constituents were confirmed using scanning electron microscopy (SEM), atomic force microscopy (AFM), Raman spectroscopy, and X-ray photoelectron spectroscopy (XPS). In addition, electrochemical charge storage was identified using cyclic voltammetry and galvanostatic cycling, where non-faradaic and faradaic contributions were isolated and analyzed. Afterward, we fabricated a sandwich cell using a PNF/MXene LbL film as the cathode and a lithium metal ribbon as the anode to measure the areal capacity, energy, and power. Finally, we discuss the mechanism of charge storage for the LbL PNF/MXene thin film and compare it to other thin-film batteries. These results demonstrate the potential application of LbL PNF/MXene thin films for energy storage devices for future use in wearable and portable small electronic devices.

2. EXPERIMENTAL SECTION

2.1. Synthesis of $Ti_3C_2T_x$ MXene Nanosheets. MXene nanosheet dispersions were prepared following previous reports.[45] The dispersion of MXene nanosheets was prepared by synthesis of Ti_3AlC_2 MAX phase powders, chemical etching of Al from the powders to obtain $Ti_3C_2T_x$ MXene clay by selective etching, followed by intercalation and delamination of $Ti_3C_2T_x$ (see the Supporting Information section and previously published studies[44−47]).

2.2. Preparation of PNF Dispersion. PNFs were synthesized according to a published procedure.[48] Aniline (1.49 g, 16 mmol) and ammonium peroxydisulfate (0.915 g, 4 mmol) were dissolved in separate HCl solutions (1 M, 50 mL). Both solutions were stirred under argon atmosphere for 1 h at room temperature. The two solutions were quickly mixed using a syringe, and the mixture turned green after a few minutes. To remove the acid, the PNF dispersion was transferred to a dialysis tube and dialyzed against 18.2 MΩ deionized water for 14 days with the water being changed twice each day. After dialysis, a total of 400 mL of PNF dispersion was obtained by diluting the PNF dispersion in deionized water. After 3 h of bath sonication, the pH of the PNF dispersion was adjusted to 2.5 using HCl. As reported by the Yun group, the concentration of PNF dispersion at that time was 0.5 mg mL^{-1}.[29]

2.3. Preparation of PNF/MXene LbL Thin Films. Prior to LbL deposition, glass and ITO-coated glass (indium tin oxide, R_s: 5−15 Ω, Delta Technologies) were cleaned with water, acetone, and isopropyl alcohol. After rinsing, all substrates were dried using nitrogen. Cleaned substrates were immersed in the PNF dispersion (0.5 mg mL^{-1}) for 15 min. The substrates were subsequently rinsed in three separate deionized water baths for 2, 1, and 1 min to remove loosely adhered PNF. After the rinsing process, the substrates were dried using nitrogen. Then, the substrates were immersed in the MXene dispersion (1.0 mg mL^{-1}) for 15 min, followed by the previous rinsing

DOI: 10.1021/acsami.9b16692
ACS Appl. Mater. Interfaces 2019, 11, 47929−47938

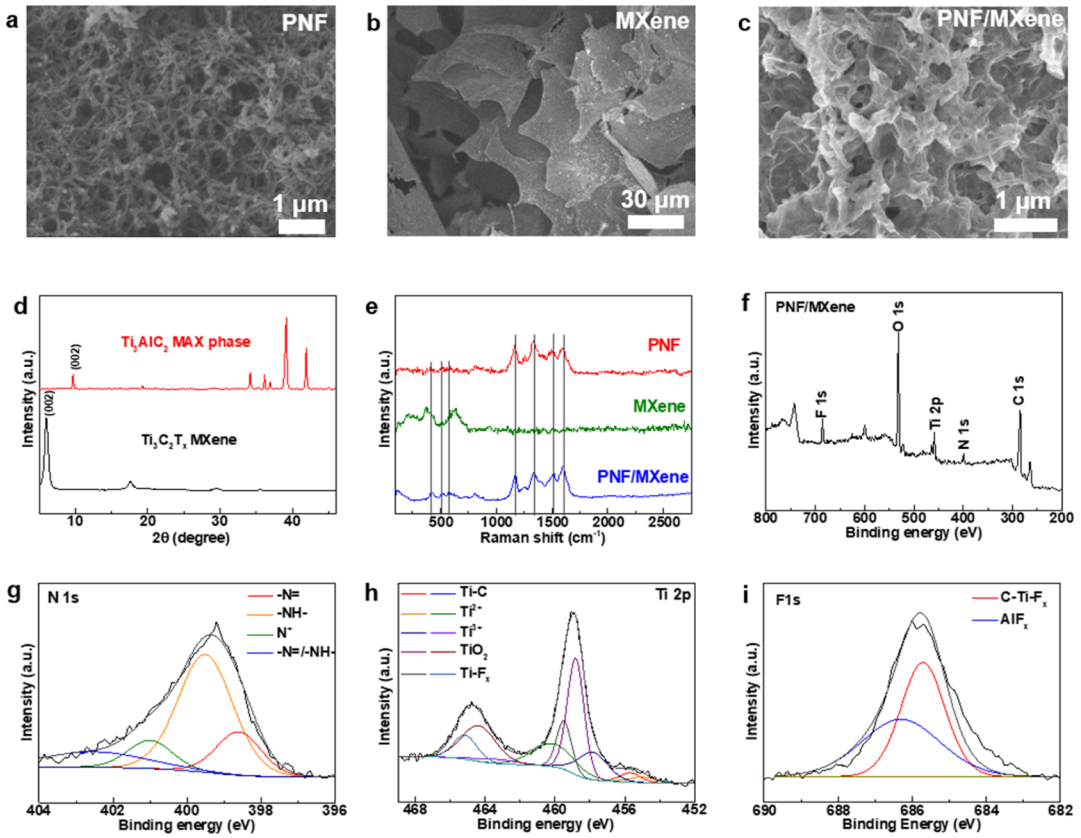

Figure 2. Characteristics of PNF/MXene multilayer electrodes. SEM images of drop-cast (a) PNFs and (b) MXenes and (c) 40 LP PNF/MXene multilayer. (d) X-ray diffraction patterns of Ti_3AlC_2 MAX phase (red) and $Ti_3C_2T_x$ MXenes (black). (e) Raman spectra of PNFs (red), MXenes (green), and a PNF/MXene multilayer (blue). (f) XPS survey spectra of a PNF/MXene multilayer and the component peak fits for (g) N 1s, (h) Ti 2p, and (i) F 1s.

and drying steps. The above procedure constituted one layer pair (LP) and was repeated until the desired number of LPs was obtained.

2.4. Characterization. UV−vis spectroscopy (SolidSpec-3700 Shimadzu) was performed over a wavelength range of 300−800 nm. In order to obtain the mass composition of the PNF/MXene LbL film, quartz crystal microbalance (QCM, Inficon, Maxtek RQCM) testing was conducted using a 5 MHz Ti/Au quartz crystal. Before LbL assembly, the substrates were plasma-treated (Harrick PDC32G) for 10 min. The composition and mass of the PNF/MXene multilayer were determined by monitoring the frequency changes for each layer deposited from 0 to 20 LPs. Profilometry (D-100, KLA-Tencor) was used to measure the thickness and roughness of the thin films. Measurements were taken at 12 different locations over an area of 4.5 cm^2. SEM (JEOL JSM-7500F) and AFM (Bruker Dimension Icon AFM in tapping mode) were used to investigate the morphologies of drop-cast PNFs, MXenes, and multilayer films. For SEM image analysis, PNFs and MXenes were prepared by drop-casting each solution onto a silicon substrate and air-drying. X-ray diffraction patterns (a Bruker D8 Powder X-ray diffractometer fitted with a LYNXEYE detector) of the MAX phase and MXenes were obtained in a Bragg−Brentano geometry with Cu Kα (λ = 1.5418 Å) radiation source. Raman spectra were recorded using a HORIBA Jobin Yvon LabRam Raman confocal microscope. XPS was performed using an Omicron XPS/UPS system with an Argus detector. All electrochemical tests were performed at room temperature in a water- and oxygen-free argon-filled glovebox. Electrochemical properties such as areal capacity, power, and energy were calculated from cyclic voltammograms and galvanostatic charge−discharge curves, see the Supporting Information. The active area of the LbL film on ITO substrate was 1.5 cm^2.

3. RESULTS AND DISCUSSION

For the long-term application of coatings as electrodes for conformal energy and power systems, LbL assembly is of utility because it produces conformal coatings on a variety of substrates, regardless of chemistry and topography.[4,10,16,41,42,49] One of the challenges with thin-film electrodes is the mechanical stability of the electrode, especially when using powdery materials such as PNFs. Here, the MXene nanosheets provided binding through the electrostatic interactions that enhanced mechanical stability, relative to PNFs alone (Figure S1).

Figure 1 shows a schematic of the LbL assembly of positively charged PNFs and negatively charged MXenes into a multilayer film. The pH values of the PNF and MXene dispersions were 2.5 and 5.6, respectively. We fabricated PNF/MXene multilayer films for chemical and electrochemical analysis on glass slide substrates (Figure 1b) and ITO-coated glass (Figure S2), respectively. The number of PNF/MXene LPs ranged from 0 to 40, and images of the PNF/MXene multilayers were taken every five layers (Figure 1b). The five LP PNF/MXene film displayed a bluish green appearance and gradually became darker as the number of LPs increased. This bluish green color resulted from the conductive emeraldine state of the PNFs.[50] Figure 1c shows the UV−vis spectra for PNF/MXene multilayers for varying LP number; the broad peak near 630 nm arose from the exciton transition of the quinoid rings in PNFs.[51,52] In addition, this peak increased with increasing number of LP. Figure 1d shows the UV absorbance value at 630 nm as a function of LP number,

DOI: 10.1021/acsami.9b16692
ACS Appl. Mater. Interfaces 2019, 11, 47929−47938

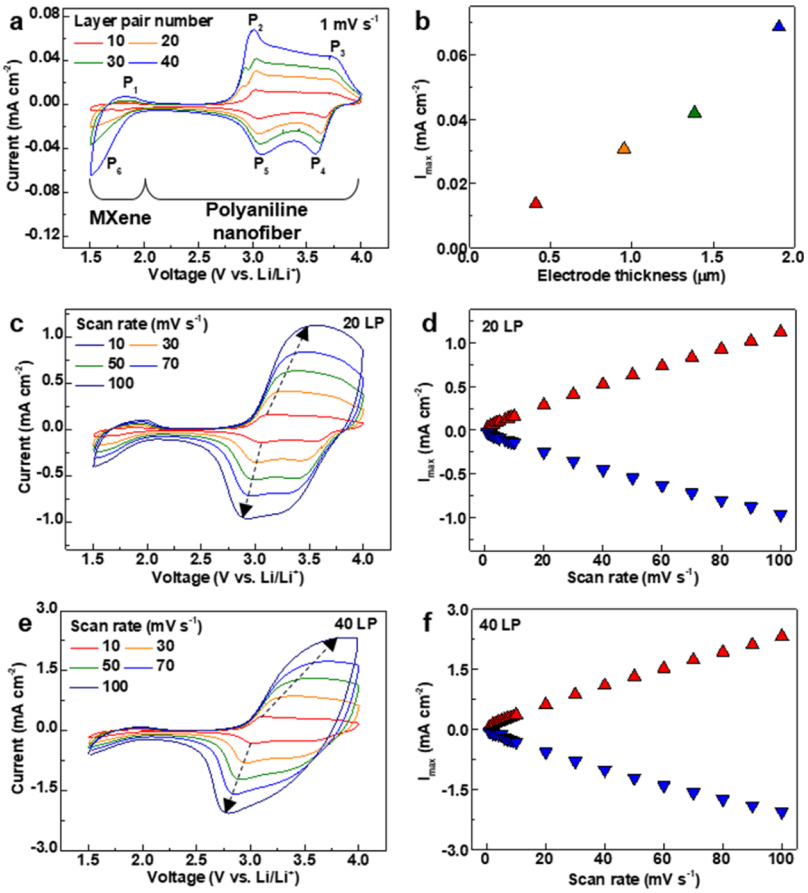

Figure 3. (a) Cyclic voltammograms of PNF/MXene LbL electrodes of varying number of LP at a scan rate of 1 mV s^{-1}. (b) Maximum current vs electrode thickness taken from cyclic voltammograms. Cyclic voltammograms of (c) 20 LP and (e) 40 LP of PNF/MXene LbL electrodes at scan rates of 10, 30, 50, 70, and 100 mV s^{-1}. Maximum current of (d) 20 LP and (f) 40 LP of PNF/MXene LbL electrodes taken from the corresponding cyclic voltammograms (three-electrode cell: lithium ribbons as counter and reference electrodes, 1 M $LiClO_4$ dissolved in propylene carbonate as an electrolyte).

indicating that the absorbance increases linearly with the LP number. From QCM, we determined that the deposited mass of the PNF/MXene multilayer film gradually increased (3.05 μg cm^{-2} per LP) (Figure S3). Additionally, the mass percentages of PNFs and MXenes in the film were determined to be 77 and 23%, respectively. Figure S4 shows the thickness and roughness as a function of the number of LPs. Figure S4a indicates that the thickness increased linearly with increasing LPs (49 nm per LP), as with absorbance and QCM data. Previous studies have reported that PNFs fabricated from a general chemical route have a diameter of 30−120 nm, and the thickness of $Ti_3C_2T_x$ MXene flakes synthesized by etching from the MAX phase is about 1.6 nm.[53,54] These values are reasonably less than the growth per LP. Figure S4b indicates that the surface roughness also increases with increasing number of LPs for the PNF/MXene multilayers, where roughness ranged from 400 to 980 nm. Taken together, these data indicate that the LbL assembly process is controllable as the thickness and roughness of the electrode can easily be controlled by changing the number of LPs deposited. Further, the data indicate that the electrostatic interactions between PNFs and MXene flakes are strong enough to sustain continued LbL growth.

Figure 2 presents the structural and chemical properties of the PNF/MXene multilayer film and its constituent materials, PNFs and MXenes. In Figure 2a−c, the SEM images of PNFs, MXenes, and the PNF/MXene multilayer film are displayed, respectively. Figure 2a shows drop-cast PNFs with a diameter of 50−90 nm. In Figure 2b, the MXenes have a flake-like structure with diameters >10 μm. The SEM image of the PNF/MXene multilayer depicts the formation of a porous structure containing both PNFs and MXene nanosheets (Figure 2c). The porous structure has the advantage of improving the specific surface area and efficiency of ion transport. We also compared the surface morphology of a 5 LP PNF/MXene film to that of the 40 LP PNF/MXene film using SEM and AFM (Figures S5 and S6). The surface morphology of both films was similar for both LP numbers, indicating highly reproducible and uniform layer growth of LbL assembly PNF/MXene multilayers for both methods. In addition, we examined the surface using AFM, Figure S6, which yielded results similar to profilometry.

Cross-sectional SEM images and elemental mapping provided a more detailed view of the electrode morphology. Figure S7 presents a cross-sectional SEM image of a PNF/MXene multilayer film on a Si substrate. The electrode cross section bears a structure similar to that observed in surface SEM images, in which the PNF network and MXene nanosheets were both observed. The elemental mapping of the LbL electrode in Figure S8 showed an even distribution of C, N, Ti, and F, elements present in PNFs and MXene nanosheets.

DOI: 10.1021/acsami.9b16692
ACS Appl. Mater. Interfaces 2019, 11, 47929−47938

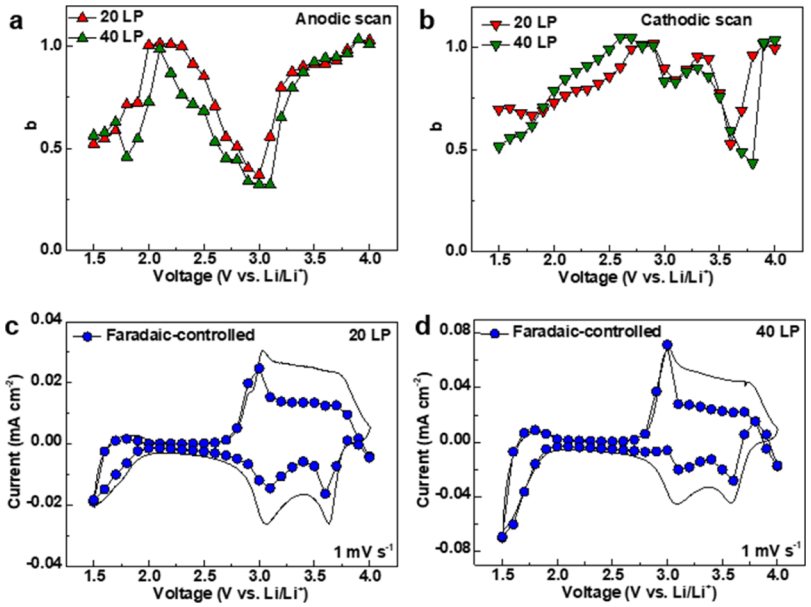

Figure 4. Calculated *b*-values vs voltage in (a) anodic and (b) cathodic scans for 20 LP and 40 LP PNF/MXene multilayers. The faradaic contribution is displayed as the blue-dotted line in the cyclic voltammograms (the black line indicates the total current) of (c) 20 LP and (d) 40 LP PNF/MXene multilayers at 1 mV s^{-1}.

Figure 2d shows the XRD patterns of the MAX phase (Ti_3AlC_2) and the MXene nanosheets ($Ti_3C_2T_x$). As described in the experimental section, MXenes were obtained through the selective etching process of the A constituent from the starting MAX phase followed by intercalation and delamination processes. The pronounced (002) peak of the MAX phase at the 2θ angle of 9.7° shifts to ~6.5° after the process.[44,55] This pronounced (002) peak also shows a tendency to broaden as the thickness increases, and the *d*-spacing of the $Ti_3C_2T_x$ layers increases through the process.[56] Figure 2e displays the Raman spectra of PNFs, MXenes, and the PNF/MXene multilayer. In the PNF Raman spectra, four major peaks were identified: 1163 cm^{-1} for C−H bending, 1331 cm^{-1} for C−N stretching, 1496 cm^{-1} for C═N stretching, and 1596 cm^{-1} for C−C stretching.[33] In the MXene Raman spectra, the peaks were observed at 415, 518, and 576 cm^{-1}. The peak at 518 cm^{-1} indicates the presence of titanium oxide in the anatase phase, and the peaks at 415 and 579 cm^{-1} indicate the presence of titanium oxide in the rutile phase.[57] The presence of titanium oxide is discussed below. For the PNF/MXene multilayer, it is confirmed that the PNF and MXene Raman spectra peaks are present at the same time, which indicates that the PNF/MXene multilayer film is stably manufactured through the LbL assembly process.

Next, we conducted XPS analyses to identify the chemical states of PNFs, MXenes, and the PNF/MXene multilayer (Figures S9, S10, and 2f–i, respectively). Figure 2f shows the survey spectrum of the PNF/MXene multilayer film for components C 1s, N 1s, Ti 2p, O 1s, and F 1s. In the case of LbL films, it was difficult to obtain an accurate deconvolution spectrum because of the overlap in the C 1s and O 1s peaks of PNFs and MXenes, respectively. Therefore, only the N 1s, Ti 2p, and F 1s spectra were deconvoluted. Figure 2g shows the deconvoluted spectrum of N 1s, which is attributed to the signature of the PNFs. The observed peaks were assigned to quinonoid imine (−N═) at 398.5 eV, benzenoid amine (−NH−) at 399.5 eV, positively charged nitrogen (N^+) at 401.1 eV, and benzenoid amine and quinonoid imine (−N═/−NH−) at 402.6 eV.[58] Figure 2h shows the deconvoluted Ti 2p spectrum with peaks for Ti^+ (Ti−C and Ti−F_x), Ti^{2+}, Ti^{3+}, and Ti^{4+} (TiO_2).[44] The detailed position and full width at half-maximum of peaks can be found in Table S1. In the Ti 2p region, Ti^{4+} (TiO_2) had a relatively low atomic fraction of 16.6%, indicating that $Ti_3C_2T_x$ was present in the LbL film with minimal oxidation due to processing in sodium L-ascorbate.[44] Figure 2i also shows the F 1s peak deconvoluted with peaks for AlF_x at 686.3 eV and C−Ti−F_x at 685.1 eV. This analysis confirms the mutual presence of PNFs and MXenes within the multilayer.

Figure 3 shows cyclic voltammograms of a PNF/MXene LbL electrode with varying LP and scan rate measured in a three-electrode configuration. The PNF/MXene multilayer was used as the working electrode, lithium ribbons were used as the counter and reference electrodes, and 1 M $LiClO_4$ dissolved in propylene carbonate was used as an electrolyte. Prior to the measurement, we conducted 10 cycles of electrode conditioning at a scan rate of 20 mV s^{-1} in a 1.5–4.0 V voltage range, as shown in Figure S11. This conditioning process promoted the penetration of electrolyte into the electrode, which caused the disappearance of irreversible peaks and the activation of reversible peaks. Irreversible peaks at 1.7 and 1.94 V appeared in the first cycle of the electrode conditioning process and diminished completely after conditioning (black circles in Figure S11), most likely related to the MXene terminal groups (hydroxyl or fluorine) reacting with Li^+ ions.[59] Figure 3a shows cyclic voltammograms of 10, 20, 30, and 40 LP PNF/MXene multilayers at a scan rate of 1 mV s^{-1}. Peaks labeled as P_1, P_2, P_3, P_4, P_5, and P_6 were observed in the anodic and cathodic scans, and no noticeable peak shift occurred even when the number of LPs increased. First, peaks P_1 and P_6 can be identified near 1.55 V of the anodic and cathodic scans, respectively, and are associated with Li^+ ions trapped within MXene sheets.[60] Next, we identify peak pairs for P_2/P_5 at 3 V and P_3/P_4 at 3.8 V, which are assigned to the leucoemeraldine/emeraldine and emeraldine/pernigraniline redox reactions of PNFs, respectively.[51] The maximum peak current was plotted

DOI: 10.1021/acsami.9b16692
ACS Appl. Mater. Interfaces 2019, 11, 47929–47938

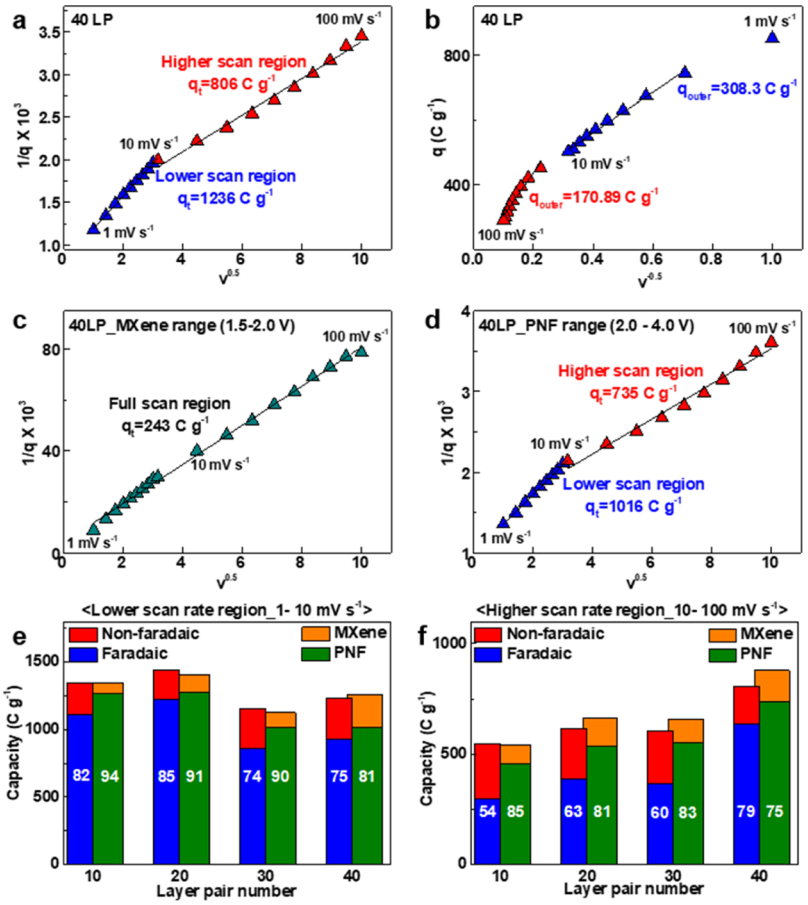

Figure 5. Graphs of (a) $1/q$ vs $v^{0.5}$ for q_t and (b) q vs $v^{-0.5}$ for q_{outer} for 40 LPs of the PNF/MXene LbL electrode. Graphs of $1/q$ vs $v^{0.5}$ for q_t of (c) voltage range assigned to the MXene nanosheets (1.5−2.0 V) and (d) voltage range assigned to the PNFs (2.0−4.0 V). Bar graph showing total capacity and the percentage contribution from non-faradaic (red) and faradaic (blue) processes and from MXenes (orange) and PNFs (olive) as a function of number of LPs at the (e) lower scan rate region (1−10 mV s^{-1}) and at the (f) higher scan rate region (10−100 mV s^{-1}).

against the thickness of the 10, 20, 30, and 40 LP PNF/MXene multilayers, demonstrating that maximum current scales linearly with thickness (Figure 3b). This indicates that the entirety of the electrode is electrochemically accessible over this range of LPs and thicknesses at a scan rate of 1 mV s^{-1}. At a higher scan rate of 30 mV s^{-1}, slight peak shifts in the anodic and cathodic directions were observed, Figure S12.

Additionally, the effect of scan rate was explored. Figure 3c,e shows cyclic voltammograms of the 20 LP and 40 LP PNF/MXene multilayers, respectively, at scan rates ranging from 10 to 100 mV s^{-1}. As the scan rate increased, no significant distortion in the response occurred, but slight peak shifts occurred because of ion transport limitations at high scan rates. Figure 3d,f shows the maximum anodic and cathodic current values for the 20 LP and 40 LP PNF/MXene multilayers with varying scan rates, respectively. These results show that the maximum anodic and cathodic currents increase linearly with increasing scan rate, which confirms that the multilayers store charge in a surface-confined redox reaction.

For a more detailed charge storage analysis, we distinguished between faradaic and non-faradaic contributions to charge storage using the following equation

$$i_d = av^b$$

where i_d is the current density (A cm^{-2}), v is the scan rate (mV s^{-1}), and a and b are dimensionless parameters.[4,61] If b is 0.5, then the redox process is considered to be an ideal faradaic process, and if b is 1, then the redox process is considered to be an ideal non-faradaic process. We calculated the b-values using the data obtained from cyclic voltammetry curves at scan rates ranging from 10 to 50 mV s^{-1}. Log i_d and log v were plotted against each other for a given potential, where b is given by the slope (Figure S13). Figure 4a,b shows plots of b versus voltage for anodic and cathodic scans of 20 LP and 40 LP PNF/MXene LbL electrodes. Figure 4a shows that the b-values of the two films obtained from the anodic scans gradually increased from 1.5 to 2.0 V. From 2.0 to 3.1 V, the b-value gradually decreased to 0.34 for 40 LP PNF/MXene LbL electrodes and 0.37 for 20 LP PNF/MXene LbL electrodes. After 3.1 V, the b-value gradually increased. The b-value obtained from the cathodic scans (Figure 4b) increased to 1.01 in the range from 1.5 to 2.9 V. This analysis suggests that charge storage within the PNF/MXene multilayer possesses both faradaic and non-faradaic character. We expect b-values to range between 0.5 and 1.0, so the excursions observed here may be interpreted qualitatively rather than quantitatively. This analysis suggests that charge storage within the PNF/MXene multilayer possesses both faradaic and non-faradaic character.

Afterward, the relative contributions of faradaic and non-faradaic charge storage were calculated using the following equation

$$i_t = a_1 v + a_2 v^{0.5}$$

DOI: 10.1021/acsami.9b16692
ACS Appl. Mater. Interfaces 2019, 11, 47929−47938

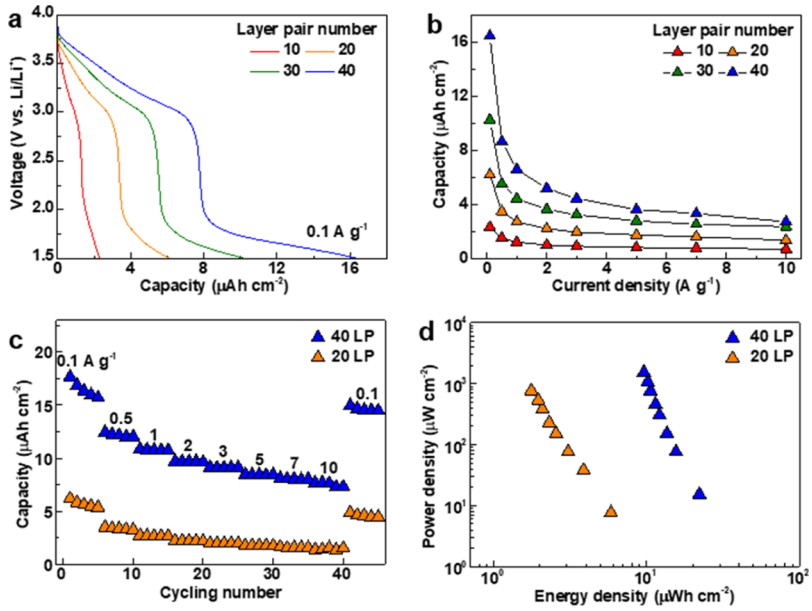

Figure 6. (a) Discharge curves for 10, 20, 30, and 40 LP PNF/MXene multilayers at a current density of 0.1 A g^{-1} in a three-electrode cell. (b) Capacity of PNF/MXene multilayers of varying LP number vs discharge current. (c) Galvanostatic cycling of 40 LP PNF/MXene multilayer in a two-electrode sandwich-type cell and (d) Ragone plot based on the surface area. Both cells used 1 M $LiClO_4$ in propylene carbonate as the electrolyte. The 40 LP multilayer was ~1.96 μm thick (Figure S4).

where i_t is the total current and a_1 and a_2 are the relative contributions of non-faradaic and faradaic processes, respectively.[4,61] Figure S14 shows plots of $i_t/v^{0.5}$ versus $v^{0.5}$ obtained at specific voltages, where the slopes and intercepts yield a_1 and a_2, respectively. From this analysis, we obtained a cyclic voltammogram at a scan rate of 1 mV s^{-1} showing the faradaic portion for 20 LP (Figure 4c) and 40 LP (Figure 4d) PNF/MXene LbL electrodes. The solid line represents the total current and the blue-dotted line represents the contribution of the faradaic process. Faradaic charge storage accounted for 57.5 and 56.1% of total charge storage for the 20 LP and 40 LP PNF/MXene LbL electrodes, respectively. Figure S15 shows the same analysis, but for a scan rate of 5 mV s^{-1}. In the case of 20 LP and 40 LP of PNF/MXene films, the faradaic charge storage decreased to 37 and 35.6%, respectively, when the scan rate increased. This demonstrates that the contribution of faradaic-controlled charge storage decreases as the scan rate increases.

Generally, electrodes with porous structures show nonuniform charge storage properties because of the scan rate dependence of the current observed during cyclic voltammetry.[62,63] This manifests as charge that is easily accessible at an outer region versus an inner region of the material within the porous structure as it is more difficult to extract charge from the interior. Thus, we applied the following equation, developed by Trasatti et al. and Shukla et al., to calculate the total maximum charge (q_t) and the fraction of charge stored at inner and outer surfaces (q_i and q_o, respectively)[61−63]

$$q_t = q_i + q_o$$

The values q_t and q_o were calculated from the intercepts of $1/q$ versus $v^{0.5}$ (Figure 5a) and q versus $v^{-0.5}$ (Figure 5b) plots, respectively, for 40 LP PNF/MXene multilayers. Two distinct linear regions were observed encompassing scan rates of 1−10 mV s^{-1} (Figure 5e) and scan rates of 10−100 mV s^{-1} (Figure 5f). Here, the values of q_i and q_o were assigned to the faradaic and non-faradaic contributions. The ratio of charge stored by faradaic and non-faradaic processes did not vary significantly with changes in LP number. The percentage of charge stored by faradaic processes was 74−85% in the lower scan rate region and 54−79% in the higher scan rate region.

We repeated this calculation for separate voltage ranges assigned to the PNF and MXene constituents (MXene: 1.5−2.0 V, PNF: 2.0−4.0 V). This allowed for the calculation of q_t, q_i, and q_o values for the corresponding voltage ranges to assign charge storage for the PNFs and MXenes individually. Figure 5c,d shows this analysis for the two voltage ranges for the LbL electrode. Figure 5c displayed a linear relationship of $1/q$ with a scan rate over the voltage range for MXenes, indicating that charge storage is predominantly non-faradaic for MXenes within the multilayer. However, Figure 5d displayed two distinct linear regions over the voltage range for PNFs similar to that observed in Figure 5a. This means that the charge storage in PNF is composed of both faradaic and non-faradaic processes. The results in Figure 5e,f show that most of the charge storage results from the electrochemical activity of the PNFs. We speculate that the presence of MXenes is advantageous because PNFs are otherwise relatively nonconducting once reduced to their leucoemeraldine state (<2.7 V). Even when PNFs are in their nonconducting state, MXenes maintain electrical percolation.

Next, galvanostatic charge−discharge measurements were performed in three-electrode cells to determine the capacities and rate capabilities of the 10 LP, 20 LP, 30 LP, and 40 LP PNF/MXene LbL electrodes at varying currents. As Kyeremateng et al. suggested in previous studies on evaluation criteria for microenergy storage devices,[64] we evaluated the electrochemical properties of LbL PNF/MXene electrodes on an areal basis. For reference, the electrochemical performances normalized for mass, thickness, area, and volume are summarized in Table S2. Figure 6a shows the discharge curves with increasing LP number at a current density of 0.1 A g^{-1}. The voltage plateau and the slope of the charge−discharge curves are consistent with the results of the cyclic voltammo-

DOI: 10.1021/acsami.9b16692
ACS Appl. Mater. Interfaces 2019, 11, 47929−47938

grams from Figure 3. As shown in Figure 6b, capacity increased with increasing LP number and gradually decreased with increasing current density. Among the electrodes, the 40 LP PNF/MXene LbL electrode possessed the highest capacity at 16.4 μA h cm^{-2}, whereas 30 LP, 20 LP, and 10 LP PNF/MXene LbL electrodes had capacities of 10.2, 6.2, and 2.3 μA h cm^{-2}, respectively. In addition, the cycling behavior of 10 LP, 20 LP, 30 LP, and 40 LP PNF/MXene LbL electrodes was assessed over 100 galvanostatic charge−discharge cycles at a current density of 10 A g^{-1} (Figure S16). The 10 LP, 20 LP, 30 LP, and 40 LP PNF/MXene LbL electrodes maintained 62, 73, 65, and 56% of their initial capacitances, respectively, after 100 charge−discharge cycles. To experimentally identify the origin of capacity fade, we made an LbL film of PNF/MXene on ITO-coated glass and compared the results before and after 100 galvanostatic charge−discharge cycles, as shown in Figure S17. The color of the electrode changed from bluish green before the cycle test to clear green after the cycle test. In SEM images of the PNF/MXene LbL surface after cycling, Figure S18, we observed two different morphologies. In the first, the electrode surface showed no significant differences after cycling (Figure S18d−f). In the second, observed elsewhere in the electrode, the PNF/MXene surface exhibited agglomerates or electrode deconstruction, Figure S18g−i. This is likely due to degradation of MXenes, which are susceptible to oxidation.

Afterward, galvanostatic charge−discharge measurements were carried out in a two-electrode sandwich cell 40 LP and 20 LP PNF/MXene multilayers (Figure 6c). The capacity showed a trend similar to that seen in the three-electrode cell configurations. The capacity values for the 40 LP cell decreased from 17.6 to 7.3 μA h cm^{-2} with increasing discharge current. After a charge−discharge cycle at 10 A g^{-1}, the capacity recovered to 15 μA h cm^{-2} at 0.1 A g^{-1}, indicating the stability of the PNF/MXene LbL electrodes. Figure 6d shows the areal energy and power of the 20 LP and 40 LP PNF/MXene LbL electrodes on a Ragone plot. The 40 LP PNF/MXene LbL electrode possessed higher specific energy and power than the 20 LP PNF/MXene LbL electrode. The 40 LP of PNF/MXene LbL electrode had a maximum areal energy of 22.1 μW h cm^{-2} at an areal power of 15.25 μW cm^{-2} and a maximum areal power of 1.5 mW cm^{-2} at an areal energy of 9.6 μW h cm^{-2}. In comparison, the 20 LP PNF/MXene LbL electrode exhibited a maximum areal energy of 5.8 μW h cm^{-2} at an areal power of 7.6 μW cm^{-2} and a maximum areal power of 759.5 μW cm^{-2} at an areal energy of 1.8 μW h cm^{-2}. These results indicate that the LbL-assembled PNF/MXene electrodes can be used for the cathodes of micro thin-film batteries or as the electrode material of microsupercapacitors. The improved performance of LbL PNF/MXene electrodes can be achieved by fabricating thicker electrodes with porous structures. We compare our work with the reported areal capacities of non-MXene-based, MXene-based, and polyaniline-based electrodes in Table S3. PNF/MXene LbL electrodes have a very low areal capacity when compared to other studies. This is because the areal capacity is highly dependent on electrode thickness, and our PNF/MXene LbL film is only 1.96 μm thick. However, when the areal capacity is calculated as the specific capacity and volumetric capacity, it can be seen that our electrodes have reasonable capacity values of 144.7 mA h g^{-1} and 92.7 mA h cm^{-3}.

4. CONCLUSIONS

In this work, we reported on the LbL assembly of PNF/MXene thin-film electrodes for the first time. Film thickness increased at a rate of 49 nm/LP with a composition of 77 wt % PNFs and 23 wt % $Ti_3C_2T_x$ MXenes. Raman spectroscopy and XPS analysis verified the presence of PNFs and MXenes, in which MXenes exhibited the presence of a small amount of TiO_2. Three-electrode measurements in the voltage range of 1.5−4.0 V (vs Li/Li$^+$) exhibited the electrochemical signatures of both PNFs and MXenes within the thin-film electrode. A detailed charge storage analysis of the PNF/MXene LbL electrodes was completed, wherein we distinguished faradaic and non-faradaic processes as well as the individual contributions of PNFs and MXenes. As expected for these two materials in a thin-film electrode, mixed contributions were observed. In a two-electrode lithium metal cell, the 40 LP PNF/MXene electrode exhibited a maximum areal capacity of 17.6 μA h cm^{-2}, a maximum areal energy of 22.1 μW h cm^{-2}, and a maximum areal power of 1.5 mW cm^{-2} for an electrode thickness of about 2 μm.

As such, we demonstrated that the LbL PNF/MXene electrode is a good candidate for thin-film electrochemical energy storage. The LbL assembly process allows highly tunable electrode thickness and conformal coatings on a variety of substrates. For future work, the performance may further be enhanced by considering the possibility of stretchable or flexible platforms or adjusting the characteristics of the obtained electrode by changing the assembly pH or ionic strength. In the future, this approach may be leveraged to assemble conformal batteries for small-scale electronic devices that will lead the fourth industrial revolution.

■ ASSOCIATED CONTENT

Supporting Information

The Supporting Information is available free of charge at https://pubs.acs.org/doi/10.1021/acsami.9b16692.

Digital images of PNF/MXene LbL films; adsorbed mass; growth profile and RMS roughness; surface SEM images of 5 LP; AFM surface characterization; cross-sectional SEM and elemental mapping images; XPS survey spectrum; electrode conditioning process; cyclic voltammograms; graphs of log i_d vs. log ν and graphs of log $i_t/\nu^{0.5}$ vs. $\nu^{0.5}$; faradaic-controlled contribution; capacity retention; optical image; SEM images of PNF/MXene 40 bilayer PNF MXene film; XPS peaks; normalized capacities; and comparison of areal capacity and volumetric capacity (PDF)

■ AUTHOR INFORMATION

Corresponding Author

*E-mail: jodie.lutkenhaus@tamu.edu.

ORCID

Micah J. Green: 0000-0001-5691-0861

Jodie L. Lutkenhaus: 0000-0002-2613-6016

Notes

The authors declare no competing financial interest.

■ ACKNOWLEDGMENTS

This material is based in part upon work supported by the National Science Foundation under grant 1760859. The authors also thank Texas A&M Energy Institute for financial

DOI: 10.1021/acsami.9b16692
ACS Appl. Mater. Interfaces 2019, 11, 47929−47938

support. Professor Zi appreciates support of the Basic Science Research Program through the National 13 Research Foundation of Korea funded by the Ministry of Science, ICT & Future Planning (no. 2017002988), and the Korea University Grant.

REFERENCES

(1) Zhang, C.; McKeon, L.; Kremer, M. P.; Park, S.-H.; Ronan, O.; Seral-Ascaso, A.; Barwich, S.; Coileáin, C. Ó.; McEvoy, N.; Nerl, H. C.; Anasori, B.; Coleman, J. N.; Gogotsi, Y.; Nicolosi, V. Additive-free MXene inks and direct printing of micro-supercapacitors. *Nat. Commun.* **2019**, *10*, 1795.

(2) Sun, H.; You, X.; Deng, J.; Chen, X.; Yang, Z.; Ren, J.; Peng, H. Novel Graphene/Carbon Nanotube Composite Fibers for Efficient Wire-Shaped Miniature Energy Devices. *Adv. Mater.* **2014**, *26*, 2868–2873.

(3) Li, H.; Li, X.; Liang, J.; Chen, Y. Hydrous RuO_2-Decorated MXene Coordinating with Silver Nanowire Inks Enabling Fully Printed Micro-Supercapacitors with Extraordinary Volumetric Performance. *Adv. Energy Mater.* **2019**, *9*, 1803987.

(4) Jeon, J.-W.; Kwon, S. R.; Lutkenhaus, J. L. Polyaniline nanofiber/electrochemically reduced graphene oxide layer-by-layer electrodes for electrochemical energy storage. *J. Mater. Chem. A* **2015**, *3*, 3757–3767.

(5) Dudney, N. J. Thin Film Microbatteries. *Electrochem. Soc. Interface* **2008**, *17*, 44–48.

(6) Simon, P.; Gogotsi, Y. Materials for electrochemical capacitors. *Nat. Mater.* **2008**, *7*, 845.

(7) Lee, S. W.; Gallant, B. M.; Byon, H. R.; Hammond, P. T.; Shao-Horn, Y. Nanostructured carbon-based electrodes: bridging the gap between thin-film lithium-ion batteries and electrochemical capacitors. *Energy Environ. Sci.* **2011**, *4*, 1972–1985.

(8) Aricò, A. S.; Bruce, P.; Scrosati, B.; Tarascon, J.-M.; van Schalkwijk, W. Nanostructured materials for advanced energy conversion and storage devices. *Nat. Mater.* **2005**, *4*, 366–377.

(9) Verger, L.; Natu, V.; Carey, M.; Barsoum, M. W. MXenes: An Introduction of Their Synthesis, Select Properties, and Applications. *Trends Chem.* **2019**, *1*, 656.

(10) An, H.; Habib, T.; Shah, S.; Gao, H.; Radovic, M.; Green, M. J.; Lutkenhaus, J. L. Surface-agnostic highly stretchable and bendable conductive MXene multilayers. *Sci. Adv.* **2018**, *4*, No. eaaq0118.

(11) Wang, H.; Wu, Y.; Yuan, X.; Zeng, G.; Zhou, J.; Wang, X.; Chew, J. W. Clay-Inspired MXene-Based Electrochemical Devices and Photo-Electrocatalyst: State-of-the-Art Progresses and Challenges. *Adv. Mater.* **2018**, *30*, 1704561.

(12) Levitt, A. S.; Alhabeb, M.; Hatter, C. B.; Sarycheva, A.; Dion, G.; Gogotsi, Y. Electrospun MXene/carbon nanofibers as supercapacitor electrodes. *J. Mater. Chem. A* **2019**, *7*, 269–277.

(13) Zhang, X.; Zhang, Z.; Zhou, Z. MXene-based materials for electrochemical energy storage. *J. Energy Chem.* **2018**, *27*, 73–85.

(14) Shahzad, F.; Alhabeb, M.; Hatter, C. B.; Anasori, B.; Man Hong, S.; Koo, C. M.; Gogotsi, Y. Electromagnetic interference shielding with 2D transition metal carbides (MXenes). *Science* **2016**, *353*, 1137.

(15) Chaudhuri, K.; Alhabeb, M.; Wang, Z.; Shalaev, V. M.; Gogotsi, Y.; Boltasseva, A. Highly Broadband Absorber Using Plasmonic Titanium Carbide (MXene). *ACS Photonics* **2018**, *5*, 1115–1122.

(16) An, H.; Habib, T.; Shah, S.; Gao, H.; Patel, A.; Echols, I.; Zhao, X.; Radovic, M.; Green, M. J.; Lutkenhaus, J. L. Water Sorption in MXene/Polyelectrolyte Multilayers for Ultrafast Humidity Sensing. *ACS Appl. Nano Mater.* **2019**, *2*, 948–955.

(17) Dong, Y.; Zheng, S.; Qin, J.; Zhao, X.; Shi, H.; Wang, X.; Chen, J.; Wu, Z.-S. All-MXene-Based Integrated Electrode Constructed by Ti_3C_2 Nanoribbon Framework Host and Nanosheet Interlayer for High-Energy-Density Li–S Batteries. *ACS Nano* **2018**, *12*, 2381–2388.

(18) Chaudhari, N. K.; Jin, H.; Kim, B.; San Baek, D.; Joo, S. H.; Lee, K. MXene: an emerging two-dimensional material for future energy conversion and storage applications. *J. Mater. Chem. A* **2017**, *5*, 24564–24579.

(19) Lukatskaya, M. R.; Mashtalir, O.; Ren, C. E.; Dall'Agnese, Y.; Rozier, P.; Taberna, P. L.; Naguib, M.; Simon, P.; Barsoum, M. W.; Gogotsi, Y. Cation Intercalation and High Volumetric Capacitance of Two-Dimensional Titanium Carbide. *Science* **2013**, *341*, 1502.

(20) Fan, Z.; Wang, Y.; Xie, Z.; Wang, D.; Yuan, Y.; Kang, H.; Su, B.; Cheng, Z.; Liu, Y. Modified MXene/Holey Graphene Films for Advanced Supercapacitor Electrodes with Superior Energy Storage. *Adv. Sci.* **2018**, *5*, 1800750.

(21) Cheng, F.; Tang, W.; Li, C.; Chen, J.; Liu, H.; Shen, P.; Dou, S. Conducting Poly(aniline) Nanotubes and Nanofibers: Controlled Synthesis and Application in Lithium/Poly(aniline) Rechargeable Batteries. *Chem.—Eur. J.* **2006**, *12*, 3082–3088.

(22) Wu, F.; Chen, J.; Chen, R.; Wu, S.; Li, L.; Chen, S.; Zhao, T. Sulfur/Polythiophene with a Core/Shell Structure: Synthesis and Electrochemical Properties of the Cathode for Rechargeable Lithium Batteries. *J. Phys. Chem. C* **2011**, *115*, 6057–6063.

(23) Jurewicz, K.; Delpeux, S.; Bertagna, V.; Béguin, F.; Frackowiak, E. Supercapacitors from nanotubes/polypyrrole composites. *Chem. Phys. Lett.* **2001**, *347*, 36–40.

(24) Mike, J. F.; Lutkenhaus, J. L. Recent advances in conjugated polymer energy storage. *J. Polym. Sci., Part B: Polym. Phys.* **2013**, *51*, 468–480.

(25) Shao, L.; Jeon, J.-W.; Lutkenhaus, J. L. Polyaniline/Vanadium Pentoxide Layer-by-Layer Electrodes for Energy Storage. *Chem. Mater.* **2012**, *24*, 181–189.

(26) MacDiarmid, A. G.; Epstein, A. J. The concept of secondary doping as applied to polyaniline. *Synth. Met.* **1994**, *65*, 103–116.

(27) Krinichnyi, V. I. The nature and dynamics of nonlinear excitations in conducting polymers. Polyaniline. *Russ. Chem. Bull.* **2000**, *49*, 207.

(28) Li, D.; Huang, J.; Kaner, R. B. Polyaniline Nanofibers: A Unique Polymer Nanostructure for Versatile Applications. *Acc. Chem. Res.* **2009**, *42*, 135–145.

(29) Qiang, J.; Yu, Z.; Wu, H.; Yun, D. Polyaniline nanofibers synthesized by rapid mixing polymerization. *Synth. Met.* **2008**, *158*, 544–547.

(30) Xu, H.; Li, X.; Wang, G. Polyaniline nanofibers with a high specific surface area and an improved pore structure for supercapacitors. *J. Power Sources* **2015**, *294*, 16–21.

(31) Li, D.; Kaner, R. B. Processable stabilizer-free polyaniline nanofiber aqueous colloids. *Chem. Commun.* **2005**, 3286–3288.

(32) Lee, S. W.; Yabuuchi, N.; Gallant, B. M.; Chen, S.; Kim, B.-S.; Hammond, P. T.; Shao-Horn, Y. High-power lithium batteries from functionalized carbon-nanotube electrodes. *Nat. Nanotechnol.* **2010**, *5*, 531.

(33) Hyder, M. N.; Lee, S. W.; Cebeci, F. Ç.; Schmidt, D. J.; Shao-Horn, Y.; Hammond, P. T. Layer-by-Layer Assembled Polyaniline Nanofiber/Multiwall Carbon Nanotube Thin Film Electrodes for High-Power and High-Energy Storage Applications. *ACS Nano* **2011**, *5*, 8552–8561.

(34) Zhang, Y.; Mu, Z.; Lai, J.; Chao, Y.; Yang, Y.; Zhou, P.; Li, Y.; Yang, W.; Xia, Z.; Guo, S. MXene/Si@SiO_x@C Layer-by-Layer Superstructure with Autoadjustable Function for Superior Stable Lithium Storage. *ACS Nano* **2019**, *13*, 2167–2175.

(35) Zeng, Z.; Xiao, F.-X.; Phan, H.; Chen, S.; Yu, Z.; Wang, R.; Nguyen, T.-Q.; Yang Tan, T. T. Unraveling the cooperative synergy of zero-dimensional graphene quantum dots and metal nanocrystals enabled by layer-by-layer assembly. *J. Mater. Chem. A* **2018**, *6*, 1700–1713.

(36) Gittleson, F. S.; Hwang, D.; Ryu, W.-H.; Hashmi, S. M.; Hwang, J.; Goh, T.; Taylor, A. D. Ultrathin Nanotube/Nanowire Electrodes by Spin–Spray Layer-by-Layer Assembly: A Concept for Transparent Energy Storage. *ACS Nano* **2015**, *9*, 10005–10017.

(37) Zhang, L.; Li, Y.; Sun, J.; Shen, J. Mechanically Stable Antireflection and Antifogging Coatings Fabricated by the Layer-by-Layer Deposition Process and Postcalcination. *Langmuir* **2008**, *24*, 10851–10857.

DOI: 10.1021/acsami.9b16692
ACS Appl. Mater. Interfaces 2019, 11, 47929–47938

(38) Xie, J.; Sun, X.; Zhang, N.; Xu, K.; Zhou, M.; Xie, Y. Layer-by-layer β-Ni(OH)$_2$/graphene nanohybrids for ultraflexible all-solid-state thin-film supercapacitors with high electrochemical performance. *Nano Energy* **2013**, *2*, 65−74.
(39) Yang, M.; Yang, Y.; Yang, H.; Shen, G.; Yu, R. Layer-by-layer self-assembled multilayer films of carbon nanotubes and platinum nanoparticles with polyelectrolyte for the fabrication of biosensors. *Biomaterials* **2006**, *27*, 246−255.
(40) Kharlampieva, E.; Kozlovskaya, V.; Sukhishvili, S. A. Layer-by-Layer Hydrogen-Bonded Polymer Films: From Fundamentals to Applications. *Adv. Mater.* **2009**, *21*, 3053−3065.
(41) Zhao, S.; Caruso, F.; Dähne, L.; Decher, G.; De Geest, B. G.; Fan, J.; Feliu, N.; Gogotsi, Y.; Hammond, P. T.; Hersam, M. C.; Khademhosseini, A.; Kotov, N.; Leporatti, S.; Li, Y.; Lisdat, F.; Liz-Marzán, L. M.; Moya, S.; Mulvaney, P.; Rogach, A. L.; Roy, S.; Shchukin, D. G.; Skirtach, A. G.; Stevens, M. M.; Sukhorukov, G. B.; Weiss, P. S.; Yue, Z.; Zhu, D.; Parak, W. J. The Future of Layer-by-Layer Assembly: A Tribute to ACS Nano Associate Editor Helmuth Möhwald. *ACS Nano* **2019**, *13*, 6151−6169.
(42) Keum, K.; Lee, G.; Lee, H.; Yun, J.; Park, H.; Hong, S. Y.; Song, C.; Kim, J. W.; Ha, J. S. Wire-Shaped Supercapacitors with Organic Electrolytes Fabricated via Layer-by-Layer Assembly. *ACS Appl. Mater. Interfaces* **2018**, *10*, 26248−26257.
(43) Lee, S. W.; Kim, B.-S.; Chen, S.; Shao-Horn, Y.; Hammond, P. T. Layer-by-Layer Assembly of All Carbon Nanotube Ultrathin Films for Electrochemical Applications. *J. Am. Chem. Soc.* **2009**, *131*, 671−679.
(44) Zhao, X.; Vashisth, A.; Prehn, E.; Sun, W.; Shah, S. A.; Habib, T.; Chen, Y.; Tan, Z.; Lutkenhaus, J. L.; Radovic, M.; Green, M. J. Antioxidants Unlock Shelf-Stable Ti3C2Tx (MXene) Nanosheet Dispersions. *Matter* **2019**, *1*, 513−526.
(45) Habib, T.; Zhao, X.; Shah, S. A.; Chen, Y.; Sun, W.; An, H.; Lutkenhaus, J. L.; Radovic, M.; Green, M. J. Oxidation stability of $Ti_3C_2T_x$ MXene nanosheets in solvents and composite films. *npj 2D Mater. Appl.* **2019**, *3*, 8.
(46) Shah, S. A.; Habib, T.; Gao, H.; Gao, P.; Sun, W.; Green, M. J.; Radovic, M. Template-free 3D titanium carbide ($Ti_3C_2T_x$) MXene particles crumpled by capillary forces. *Chem. Commun.* **2017**, *53*, 400−403.
(47) Mashtalir, O.; Naguib, M.; Mochalin, V. N.; Dall'Agnese, Y.; Heon, M.; Barsoum, M. W.; Gogotsi, Y. Intercalation and delamination of layered carbides and carbonitrides. *Nat. Commun.* **2013**, *4*, 1716.
(48) Lin, Y.-F.; Chen, C.-H.; Xie, W.-J.; Yang, S.-H.; Hsu, C.-S.; Lin, M.-T.; Jian, W.-B. Nano Approach Investigation of the Conduction Mechanism in Polyaniline Nanofibers. *ACS Nano* **2011**, *5*, 1541−1548.
(49) Carosio, F.; Alongi, J.; Malucelli, G. α-Zirconium phosphate-based nanoarchitectures on polyester fabrics through layer-by-layer assembly. *J. Mater. Chem.* **2011**, *21*, 10370−10376.
(50) Jeon, J.-W.; O'Neal, J.; Shao, L.; Lutkenhaus, J. L. Charge Storage in Polymer Acid-Doped Polyaniline-Based Layer-by-Layer Electrodes. *ACS Appl. Mater. Interfaces* **2013**, *5*, 10127−10136.
(51) Nguyen, H. D.; Nguyen, T. H.; Hoang, N. V.; Le, N. N.; Nguyen, T. N. N.; Doan, D. C. T.; Dang, M. C. pH sensitivity of emeraldine salt polyaniline and poly(vinyl butyral) blend. *Adv. Nat. Sci. Nanosci. Nanotechnol.* **2014**, *5*, 045001.
(52) Narayan, H.; Alemu, H.; Somerset, V.; Iwuoha, E.; Hernández, M.; Hernández, J.; Montaño, A.; Henao Martínez, J. *Fly Ash Composites with Polyaniline: Synthesis, Characterization and Conductivity Measurements*; Nova Science Publishers, 2009; pp 111−136.
(53) Lipatov, A.; Lu, H.; Alhabeb, M.; Anasori, B.; Gruverman, A.; Gogotsi, Y.; Sinitskii, A. Elastic properties of 2D $Ti_3C_2T_x$ MXene monolayers and bilayers. *Sci. Adv.* **2018**, *4*, No. eaat0491.
(54) Huang, J.; Kaner, R. B. A General Chemical Route to Polyaniline Nanofibers. *J. Am. Chem. Soc.* **2004**, *126*, 851−855.
(55) Li, Z.; Wang, L.; Sun, D.; Zhang, Y.; Liu, B.; Hu, Q.; Zhou, A. Synthesis and thermal stability of two-dimensional carbide MXene Ti_3C_2. *Mater. Sci. Eng., B* **2015**, *191*, 33−40.
(56) Liu, R.; Li, W. High-Thermal-Stability and High-Thermal-Conductivity $Ti_3C_2T_x$ MXene/Poly(vinyl alcohol) (PVA) Composites. *ACS Omega* **2018**, *3*, 2609−2617.
(57) Li, X.; Yin, X.; Han, M.; Song, C.; Xu, H.; Hou, Z.; Zhang, L.; Cheng, L. Ti_3C_2 MXenes modified with in situ grown carbon nanotubes for enhanced electromagnetic wave absorption properties. *J. Mater. Chem. C* **2017**, *5*, 4068−4074.
(58) Golczak, S.; Kanciurzewska, A.; Fahlman, M.; Langer, K.; Langer, J. Comparative XPS surface study of polyaniline thin films. *Solid State Ionics* **2008**, *179*, 2234−2239.
(59) Sun, D.; Wang, M.; Li, Z.; Fan, G.; Fan, L.-Z.; Zhou, A. Two-dimensional Ti_3C_2 as anode material for Li-ion batteries. *Electrochem. Commun.* **2014**, *47*, 80−83.
(60) Ahmed, B.; Anjum, D. H.; Gogotsi, Y.; Alshareef, H. N. Atomic layer deposition of SnO_2 on MXene for Li-ion battery anodes. *Nano Energy* **2017**, *34*, 249−256.
(61) Sathiya, M.; Prakash, A. S.; Ramesha, K.; Tarascon, J. M.; Shukla, A. K. V_2O_5-Anchored Carbon Nanotubes for Enhanced Electrochemical Energy Storage. *J. Am. Chem. Soc.* **2011**, *133*, 16291−16299.
(62) Ardizzone, S.; Fregonara, G.; Trasatti, S. "Inner" and "outer" active surface of RuO_2 electrodes. *Electrochim. Acta* **1990**, *35*, 263−267.
(63) Lodi, G.; Sivieri, E.; De Battisti, A.; Trasatti, S. Ruthenium dioxide-based film electrodes. *J. Appl. Electrochem.* **1978**, *8*, 135−143.
(64) Kyerematen, N. A.; Brousse, T.; Pech, D. Microsupercapacitors as miniaturized energy-storage components for on-chip electronics. *Nat. Nanotechnol.* **2016**, *12*, 7.

DOI: 10.1021/acsami.9b16692
ACS Appl. Mater. Interfaces 2019, 11, 47929−47938